The Astrophysical Journal, 988:148 (14pp), 2025 August 1 https://doi.org/10.3847/1538-4357/ade3cc

Detected Abundances of Nuclei Relative to $_{26}$Fe for Elements $_{14}$Si through $_{44}$Ru with CALET on the International Space Station

O. Adriani[1,2], Y. Akaike[3,4], K. Asano[5], Y. Asaoka[5], E. Berti[2,6], P. Betti[2,6], G. Bigongiari[7,8], W. R. Binns[9], M. Bongi[1,2], P. Brogi[7,8], A. Bruno[10], N. Cannady[11], G. Castellini[6], C. Checchia[7,8], M. L. Cherry[12], G. Collazuol[13,14], G. A. de Nolfo[10], K. Ebisawa[15], A. W. Ficklin[12], H. Fuke[15], S. Gonzi[1,2,6], T. G. Guzik[12], T. Hams[16], K. Hibino[17], M. Ichimura[18], M. H. Israel[9], K. Kasahara[19], J. Kataoka[20], R. Kataoka[21], Y. Katayose[22], C. Kato[23], N. Kawanaka[24,25], Y. Kawakubo[26], K. Kobayashi[3,4], K. Kohri[25,27], H. S. Krawczynski[9], J. F. Krizmanic[11], P. Maestro[7,8], P. S. Marrocchesi[7,8], M. Mattiazzi[13,14], A. M. Messineo[8,28], J. W. Mitchell[11], S. Miyake[29], A. A. Moiseev[11,30,31], M. Mori[32], N. Mori[2], H. M. Motz[33], K. Munakata[23], S. Nakahira[15], J. Nishimura[15], M. Negro[12], S. Okuno[17], J. F. Ormes[34], S. Ozawa[35], L. Pacini[2,6], P. Papini[2], B. F. Rauch[9], S. B. Ricciarini[2,6], K. Sakai[36], T. Sakamoto[26], M. Sasaki[11,30,31], Y. Shimizu[17], A. Shiomi[37], P. Spillantini[1], F. Stolzi[7,8], S. Sugita[26], A. Sulaj[7,8], M. Takita[5], T. Tamura[17], T. Terasawa[5], S. Torii[3], Y. Tsunesada[38,39], Y. Uchihori[40], E. Vannuccini[2], J. P. Wefel[12], K. Yamaoka[41], S. Yanagita[42], A. Yoshida[26], K. Yoshida[19], and W. V. Zober[9]

The CALET Collaboration

[1] Department of Physics, University of Florence, Via Sansone, 1-50019, Sesto Fiorentino, Italy
[2] INFN Sezione di Firenze, Via Sansone, 1-50019, Sesto Fiorentino, Italy
[3] Waseda Research Institute for Science and Engineering, Waseda University, 17 Kikuicho, Shinjuku, Tokyo 162-0044, Japan
[4] JEM Utilization Center, Human Spaceflight Technology Directorate, Japan Aerospace Exploration Agency, 2-1-1 Sengen, Tsukuba, Ibaraki 305-8505, Japan
[5] Institute for Cosmic Ray Research, The University of Tokyo, 5-1-5 Kashiwa-no-Ha, Kashiwa, Chiba 277-8582, Japan
[6] Institute of Applied Physics (IFAC), National Research Council (CNR), Via Madonna del Piano, 10, 50019, Sesto Fiorentino, Italy
[7] Department of Physical Sciences, Earth and Environment, University of Siena, via Roma 56, 53100 Siena, Italy
[8] INFN Sezione di Pisa, Polo Fibonacci, Largo B. Pontecorvo, 3-56127 Pisa, Italy
[9] Department of Physics and McDonnell Center for the Space Sciences, Washington University, One Brookings Drive, St. Louis, MO 63130-4899, USA; wzober@wustl.edu
[10] Heliospheric Physics Laboratory, NASA/GSFC, Greenbelt, MD 20771, USA
[11] Astroparticle Physics Laboratory, NASA/GSFC, Greenbelt, MD 20771, USA
[12] Department of Physics and Astronomy, Louisiana State University, 202 Nicholson Hall, Baton Rouge, LA 70803, USA
[13] Department of Physics and Astronomy, University of Padova, Via Marzolo, 8, 35131 Padova, Italy
[14] INFN Sezione di Padova, Via Marzolo, 8, 35131 Padova, Italy
[15] Institute of Space and Astronautical Science, Japan Aerospace Exploration Agency, 3-1-1 Yoshinodai, Chuo, Sagamihara, Kanagawa 252-5210, Japan
[16] Center for Space Sciences and Technology, University of Maryland, Baltimore County, 1000 Hilltop Circle, Baltimore, MD 21250, USA
[17] Kanagawa University, 3-27-1 Rokkakubashi, Kanagawa, Yokohama, Kanagawa 221-8686, Japan
[18] Faculty of Science and Technology, Graduate School of Science and Technology, Hirosaki University, 3, Bunkyo, Hirosaki, Aomori 036-8561, Japan
[19] Department of Electronic Information Systems, Shibaura Institute of Technology, 307 Fukasaku, Minuma, Saitama 337-8570, Japan
[20] School of Advanced Science and Engineering, Waseda University, 3-4-1 Okubo, Shinjuku, Tokyo 169-8555, Japan
[21] National Institute of Polar Research, 10-3, Midori-cho, Tachikawa, Tokyo 190-8518, Japan
[22] Faculty of Engineering, Division of Intelligent Systems Engineering, Yokohama National University, 79-5 Tokiwadai, Hodogaya, Yokohama 240-8501, Japan
[23] Faculty of Science, Shinshu University, 3-1-1 Asahi, Matsumoto, Nagano 390-8621, Japan
[24] Department of Physics, Graduate School of Science, Tokyo Metropolitan University, 1-1 Minamii-Osawa, Hachioji, Tokyo 192-0397, Japan
[25] National Astronomical Observatory of Japan, 2-21-1 Osawa, Mitaka, Tokyo 181-8588, Japan
[26] Department of Physical Sciences, College of Science and Engineering, Aoyama Gakuin University, 5-10-1 Fuchinobe, Chuo, Sagamihara, Kanagawa 252-5258, Japan
[27] Institute of Particle and Nuclear Studies, High Energy Accelerator Research Organization, 1-1 Oho, Tsukuba, Ibaraki 305-0801, Japan
[28] University of Pisa, Polo Fibonacci, Largo B. Pontecorvo, 3-56127 Pisa, Italy
[29] Department of Electrical and Computer Engineering, National Institute of Technology (KOSEN), Gifu College, 2236-2 Kamimakuwa, Motosu-city, Gifu 501-0495, Japan
[30] Center for Research and Exploration in Space Sciences and Technology, NASA/GSFC, Greenbelt, MD 20771, USA
[31] Department of Astronomy, University of Maryland, College Park, MD 20742, USA
[32] Department of Physical Sciences, College of Science and Engineering, Ritsumeikan University, Shiga 525-8577, Japan
[33] Faculty of Science and Engineering, Global Center for Science and Engineering, Waseda University, 3-4-1 Okubo, Shinjuku, Tokyo 169-8555, Japan
[34] Department of Physics and Astronomy, University of Denver, Physics Building, Room 211, 2112 East Wesley Avenue, Denver, CO 80208-6900, USA
[35] Quantum ICT Advanced Development Center, National Institute of Information and Communications Technology, 4-2-1 Nukui-Kitamachi, Koganei, Tokyo 184-8795, Japan
[36] Kavli Institute for Cosmological Physics, The University of Chicago, 5640 South Ellis Avenue, Chicago, IL 60637, USA
[37] College of Industrial Technology, Nihon University, 1-2-1 Izumi, Narashino, Chiba 275-8575, Japan
[38] Graduate School of Science, Osaka Metropolitan University, Sugimoto, Sumiyoshi, Osaka 558-8585, Japan
[39] Nambu Yoichiro Institute for Theoretical and Experimental Physics, Osaka Metropolitan University, Sugimoto, Sumiyoshi, Osaka 558-8585, Japan
[40] National Institutes for Quantum and Radiation Science and Technology, 4-9-1 Anagawa, Inage, Chiba 263-8555, Japan
[41] Nagoya University, Furo, Chikusa, Nagoya 464-8601, Japan
[42] College of Science, Ibaraki University, 2-1-1 Bunkyo, Mito, Ibaraki 310-8512, Japan
Received 2025 April 14; revised 2025 June 9; accepted 2025 June 10; published 2025 July 21

Abstract

The Calorimetric Electron Telescope (CALET), launched to the International Space Station (ISS) in 2015 August and continuously operating since, measures cosmic-ray (CR) electrons, nuclei, and gamma rays. CALET, with its 27 radiation length deep Total Absorption Calorimeter, measures particle energy and allows for the measurement of spectra, secondary to primary ratios of the more abundant CR nuclei through $_{28}$Ni, while the main charge detector can measure ultra-heavy CR nuclei through $_{44}$Ru. The results for the abundances of elements from $Z = 14$ to $Z = 44$ relative to $_{26}$Fe over 7.5 yr of observation are presented here and compared to previous measurements from ACE-CRIS, SuperTIGER, and HEAO-3.

Unified Astronomy Thesaurus concepts: Particle astrophysics (96); Galactic cosmic rays (567); Interstellar medium (847)

1. Introduction

The study of the abundances of isotopes and elements in galactic cosmic rays (GCRs) can provide insight into their origins and constraints. How the Galaxy produces and distributes the elements is an open astrophysical question that still requires experimental input. Since the joint detection of GW170817 in gravitational waves (B. P. Abbott et al. 2017), GRB 170817A in gamma rays, and the subsequent kilonova observed at optical wavelengths (B. P. Abbott et al. 2017), debate about where and how the heaviest atomic nuclei are created across the Galaxy has been reinvigorated.

The measurement of ultra-heavy galactic cosmic rays (UHGCR), $_{26}$Fe and higher charge elements, provides insight into the origins of cosmic rays. UHGCRs come from outside the heliosphere but within the Milky Way, and are produced and accelerated in some of the most energetic processes in our Galaxy, such as supernovae (SNe; J. C. Higdon & R. E. Lingenfelter 2005; R. E. Lingenfelter 2019; N. de Séréville et al. 2024) and binary neutron star merger events (S. Fujibayashi et al. 2023; A. Bandyopadhyay et al. 2024), along with more exotic sources such as magnetar flares (A. Patel et al. 2025). The relative abundances of UHGCR can be used to probe processes of their production, but one cannot directly associate cosmic rays with their source, as their arrival directions are made isotropic in their propagation by the galactic magnetic field. However, the composition measurement can provide unique (or invaluable) information for understanding the processes that create GCRs.

In general, measurements of GCR abundances have found that the nuclear composition of GCRs is dominated by lighter species of nuclei produced in both stellar and primordial processes (K. Lodders 2003). The majority of the cosmic-ray flux is hydrogen (∼89%) and helium (∼10%) nuclei. All other elements make up that final percentage, with the heaviest being incredibly rare. For these ultra-heavy (UH) elements that are heavier than $_{26}$Fe, the relative rarity at the highest charges means that most absolute UHGCR individual elemental abundances are difficult to obtain.

Single-element resolution measurements above $_{26}$Fe have been made by only a small number of instruments. Antarctic balloon-borne measurements have been made up to $_{40}$Zr by TIGER (B. F. Rauch et al. 2009) and up to $_{56}$Ba by SuperTIGER (N. E. Walsh et al. 2021) at ∼GeV/nuc energies, while single-element space-based measurements have been published up to $_{38}$Zr by the ACE-CRIS (W. R. Binns et al. 2022) instrument at hundreds of MeV/nuc. The HEAO-3 instrument (W. R. Binns et al. 1989) has also published results at ∼GeV/nuc energies but only has single-element resolution up to $_{32}$Ge before transitioning to odd–even pairs of nuclei to $Z = 60$. These space-based and balloon-based experiments have different systematic effects that must be accounted for, which result in unique corrections for energy loss and nuclear interactions in the atmosphere or deflection by the geomagnetic field.

In Figure 1, the relative abundances of elements ($1 \leqslant Z \leqslant 56$) for cosmic rays with energies of $\sim$2 GeV nucleon^{-1} are compared with Solar System (SS) abundances normalized to $_{14}$Si. The two samples are largely consistent. The differences seen below $_{26}$Fe are understood to mainly arise from spallation occurring during GCR propagation between source and detection. This spallation increases the less prevalent secondary element abundances through the erosion of heavier primary nuclei, increasing the abundances of those secondary GCR compared to those seen in the SS. These differences can be studied to probe models of propagation and constrain source properties.

Some models suggest that the majority of GCR originate from OB associations, where many young, massive stars of spectral type O and B reside, leading to a high rate of SNe that occur in close proximity to one another (J. C. Higdon and R. E. Lingenfelter 2005 and references therein). These SNe produce shock waves that sweep up and accelerate GCRs to energies sufficient to escape their local OB association and propagate through the interstellar medium (ISM). This results in GCRs being composed of ISM and massive star material (MSM) produced via stellar winds and previous SN explosions within the OB association.

GCR can also be broken down by volatility (R. I. Epstein 1980), the temperature at which elements are likely to form interstellar dust grains. One theory suggests that the refractory elements (condensation temperatures, $T_c > 1250$ K, as in D. C. Ellison et al. 1997) are enhanced relative to volatile elements ($T_c < 1250$ K) in abundances measurements. The idea proposed is that elements likely to form in interstellar dust grains should be preferentially accelerated over those that exist primarily as interstellar gasses, as diffuse shock acceleration is more efficient for particles with higher rigidity. The higher mass-to-charge ratio of interstellar dust grains would have a higher rigidity than individual nuclei in interstellar gasses, allowing them to be accelerated more readily, and this enhancement would follow a mass-dependent trend (R. E. Lingenfelter 2019). The aforementioned SuperTIGER results of N. E. Walsh et al. (2021) sees this model work up to $Z = 40$, after which the volatile *r*-process nuclei have an enhancement. This enhancement suggests there may be a break in the volatility model or an inclusion of additional *r*-process nuclei sources. For further understanding of the origins of the break in this model, more GCR abundances in this region of charge would be needed.

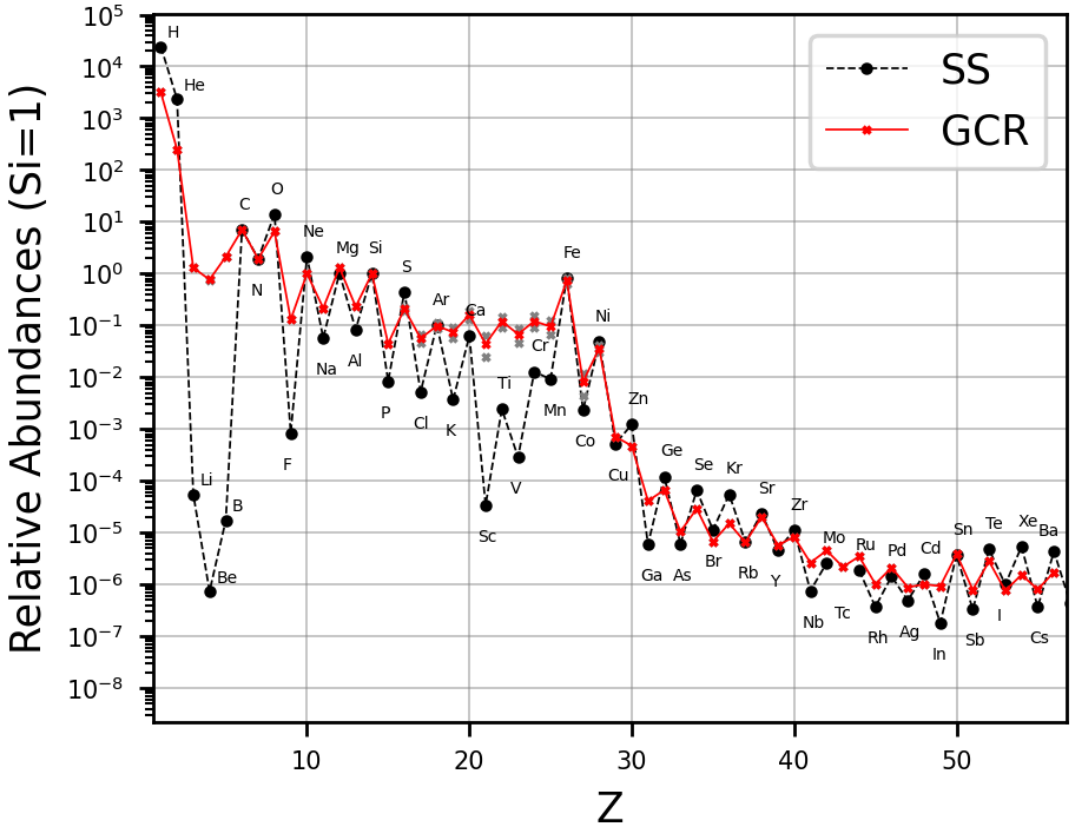

Figure 1. SS (K. Lodders 2003) and GCR relative abundances at ∼2 GeV nuc^{-1}. GCR data are sourced for $1 \leqslant Z \leqslant 2$ from T. Sanuki et al. (2000), $Z = 3$ from M. Aguilar et al. (2011), $4 \leqslant Z \leqslant 28$ from J. J. Engelmann et al. (1990), $Z = 29$ from B. F. Rauch et al. (2009), and $28 \leqslant Z \leqslant 56$ from N. E. Walsh et al. (2021), and normalized to $_{14}$Si.

2. The CALET Instrument

The CALorimetric Electron Telescope (CALET; S. Torii & P. S. Marrocchesi 2019; Y. Akaike et al. 2024) was launched in 2015 and mounted onto port 9 of the Japanese Experiment Module—Exposed Facility (JEM-EF) on the International Space Station (ISS) with a principal science goal to measure the spectrum of the all-electron flux ($e^- + e^+$) up to TeV energies. CALET was designed to effectively determine particle type and energy, with a normal incidence depth of 30 radiation lengths (X_0) to measure the highest-energy electrons. This design also provides the ability to maximize electromagnetic shower containment for background rejection and a dynamic range for measuring elemental charge up to and beyond $Z = 40$.

The CALET calorimeter is composed of three subsystems: the Charge Detector (CHD), the Imaging Calorimeter (IMC), and the Total Absorption Calorimeter (TASC; Figure 2(a)). The CHD is designed for charge identification and comprises two orthogonal layers of plastic scintillating paddles read out by photomultiplier tubes (PMTs). Each paddle is 32 mm (W) × 450 mm (L) × 10 mm (T). The CHD has a charge resolution of 0.15 electron charge units (e) for low Z elements like $_5$B to ∼0.3–0.35 e for UH elements above $_{26}$Fe (Y. Asaoka et al. 2017).

The IMC is designed to determine particle trajectory via eight pairs of x-y layers of square plastic scintillating fibers. These layers are significantly finer than the CHD paddles—each fiber has a 1 mm^2 cross section. Fibers from pairs of layers along the same axis (e.g., the first two IMC X layers) are read out in each layer by 14 64-channel multianode PMTs (MAPMTs). Tungsten sheets are placed between successive sets of x-y layers in the IMC to induce particle showers within the detector. The top five sheets are 0.7 mm thick, and the lower two are 3.5 mm thick. In total, the IMC is ∼3 X_0 thick. The showers generated in the IMC allow the high spatial resolution to be leveraged for particle trajectory and determination and the measurement of energy within the TASC.

The TASC itself comprises six pairs of orthogonal x-y layers of lead tungstate ($PbWO_4$) logs. Each layer has 16 logs that are 19 mm (W) × 326 mm (L) × 20 mm (H). In total, the TASC is 27 X_0 thick at normal incidence. The topmost layer uses PMTs for readout and contributes to the event trigger logic, while the remaining layers use a combination of photodiodes (PD) and avalanche photodiodes (APD). The PD/APD sensors have four overlapping, cross-calibrated gain ranges, giving the TASC a large dynamic range of six orders of magnitude for measuring the deposited energy.

The total 30 X_0 depth of CALET provides for a near total containment of electromagnetic showers up to 10s of TeV for electrons and photons. For protons, the calorimeter only has a depth of 1.3 interaction lengths, and a considerable fraction of shower energy is lost due to the escape of secondary hadrons (such as pions) created in nuclear interactions, from the edges of the detector. This interaction length decreases as a function of increasing Z resulting in smaller fractions of energy being contained. These differences in interaction length result in

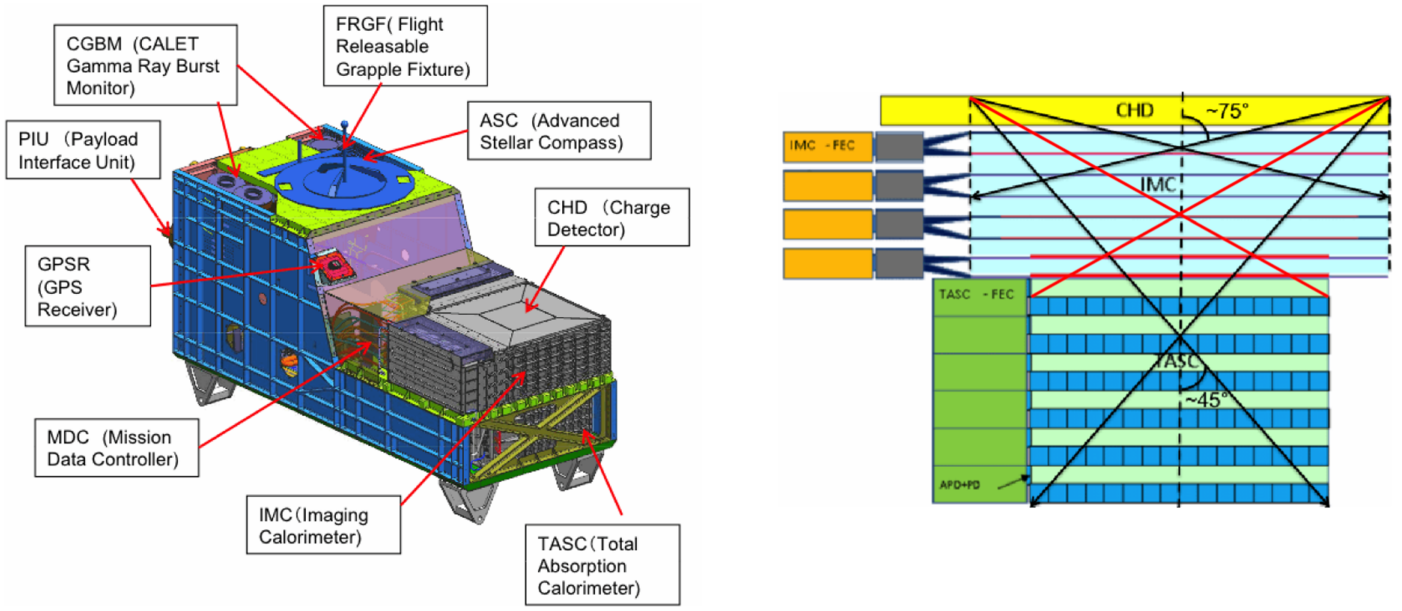

Figure 2. The left panel (a) shows a schematic of the CALET payload. CALET consists of the Main Calorimeter, which has three elements: the Charge Detector (CHD), the Imaging Calorimeter (IMC), and the Total Absorption Calorimeter (TASC). CALET also has the Gamma Ray Burst Monitor (CGBM) and several support sensors and subsystems that include the Advanced Stellar Compass (ASC), the GPS Receiver (GPSR), and the Mission Data Controller (MDC), which controls the CALET detectors and acquires the data from the instruments. The right panel (b) shows the structure of the CAL subdetectors, CHD, IMC, and TASC, with the maximum acceptance angle for UH events in the overall UH trigger, the TASC UH analysis subset entry boundary (red), and maximum angle for passing through the entirety of the detector.

different shower characteristics for electromagnetic and hadronic primaries, giving separation power between the two.

One effect of this lack of containment is coarser energy resolution for protons and heavier nuclei. To determine the energy of those events, the energy scale was calibrated via prelaunch beam test model development and validation, and the response was updated with ongoing on-orbit performance characterization and simulations of detector response. With these procedures combined, the energy spectrum for individual hadronic species can be "unfolded" from the spectrum of TASC-deposited energies.

For the analysis shown in this work, the individual layers are denoted by appending an X or Y for the IMC and TASC to the end of the subsystem name, i.e., CHDX and CHDY correspond to the x and y layers of the CHD and a label such as TASCX0 corresponds to the top X layer of the TASC. The X layer is always above the paired Y layer, and it should also be noted that for detectors with more than one layer, the layer numbers start at 0.

In previous work (B. Rauch et al. 2017; W. V. Zober et al. 2021), it has been stated that these UH measurements would only be possible for $Z \leqslant 40$. This was primarily based on conservative assumptions that the analog-to-digital converters (ADCs) in the signal chain would begin to saturate after $Z = 45$ for incidence angles exceeding 45° and higher-Z nuclei would saturate the signal chain at increasingly shallower angles until around $Z = 56$, which saturates at vertical incidence. (B. F. Rauch et al. 2011). The rigidity analysis, with its wider 75° acceptance limit, expects saturation slightly above $Z = 40$. The TASC analysis is bound by a ~60° acceptance limit, which places the maximum Z near $Z = 45$. This should also not be taken as a suggestion that Z exceeding the saturation limit cannot be measured but that significant work would need to be done to determine the correct charge. Since CALET has a relatively small geometry factor compared to SuperTIGER, there are also not enough events to fully validate any correction used in a charge extension above the saturation limit.

CALET is sensitive to a similar energy range as TIGER and SuperTIGER, but the measured abundances from the different experiments require corrections for different systematic effects. The balloon-based observations from TIGER and SuperTIGER must be corrected for energy losses and nuclear interactions that occur in the residual overhead atmosphere, while measurements from the ISS are subject to geomagnetic screening and interactions with mobile ISS structures occasionally crossing the field of view. The TIGER/SuperTIGER measurements do not have this systematic effect, as the geomagnetic cutoff above Antarctica is lower than the minimum energy thresholds of the detector. In comparison, UHGCR observations by ACE-CRIS were made outside the geomagnetic field but in a lower energy range. While the ACE-CRIS and SuperTIGER instruments have measured down to $_5$B and $_{10}$Ne, respectively, CALET can provide a cross-check on their results via an additional measurement of cosmic-ray abundances in the $14 \leqslant Z \leqslant 44$ charge range.

3. Methods

The uniform conversion of digitized signals from the CHD, IMC, and TASC to the corresponding deposited energies requires frequent calibration. CALET was calibrated prior to flight based on the results from beam tests at CERN, and instrument response parameter trends are monitored and updated throughout the mission. Further details on operations and calibrations can be found in Y. Asaoka et al. (2018) and Y. Asaoka et al. (2017), respectively.

The event-triggering logic in CALET is divided into three simultaneously active hardware trigger modes: single particle, low energy, and high energy. Trigger primitives are sent from the CHD, IMC MAPMT sums, and top TASC layer. Multiple

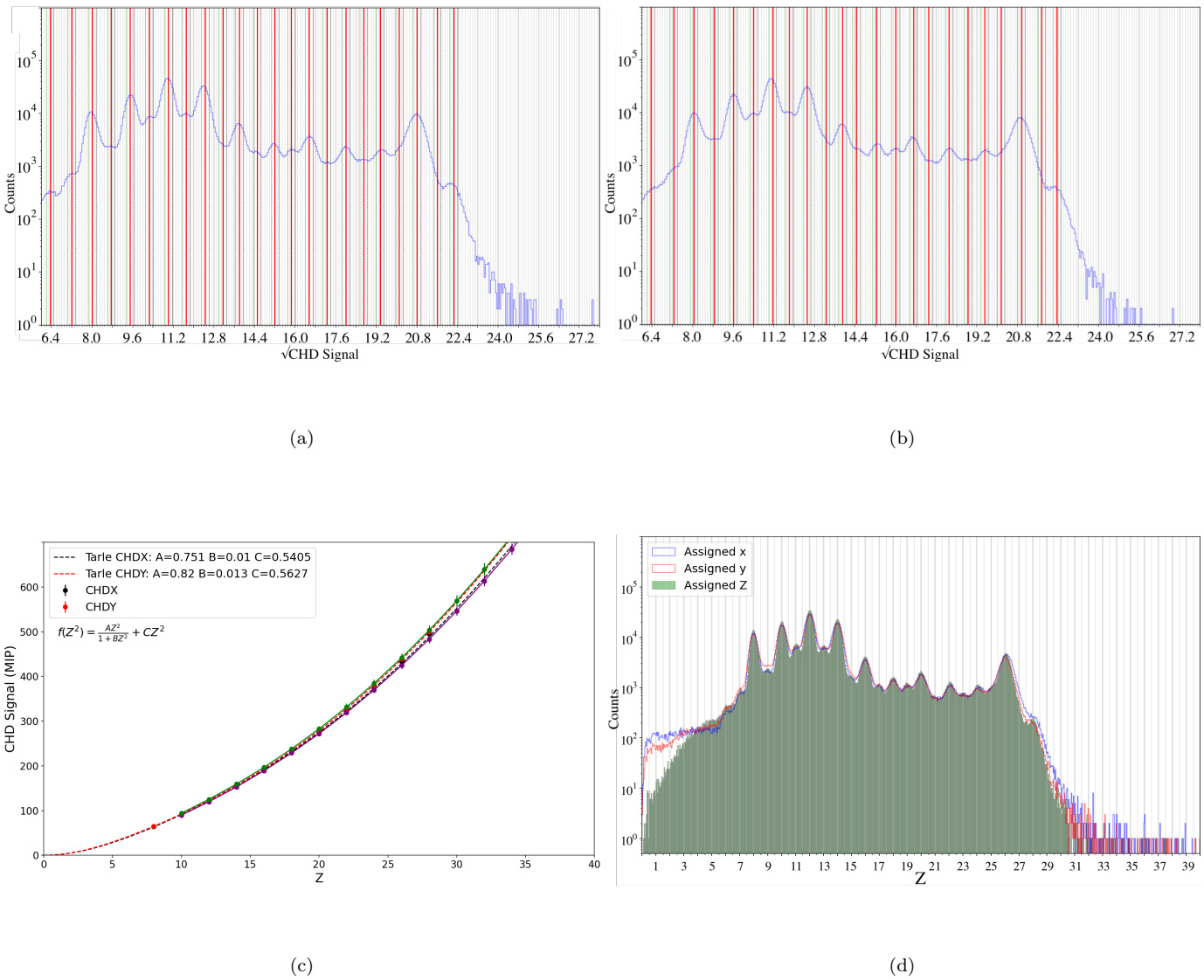

Figure 3. Step-by-step results of a peak fit routine for CHDX (a) and CHDY (b) for the 10th energy bin. Red lines indicate the determined peak position, with dashed lines designating the full region of allowed peak locations. (c) Simplified Tarle equation for CHDX in black compared to expected values based on parameters in the CALET $_{26}$Fe analysis in purple. CHDY is in red, with expected values in green. Error bars on expected values are defined by varying the parameters within 1σ of the Tarle fit in the CALET $_{26}$Fe analysis and taking the maximum and minimum CHD signal for that Z. (d) Determined Z from Tarle model fit to assign charge for CHDX in blue and CHDY in red, with the average Z overlaid in green shading.

run modes are configured for these hardware triggers (except the high-energy shower mode, which is always active for CALET primary science) via flight-configurable discriminator thresholds. One such run mode is dedicated to heavy nuclei. This trigger mode requires a high threshold in the CHD and does not require passage through the lower half of the IMC or the top of the TASC. This run mode, the UH trigger, is the focus of this work. The full details of the CALET triggering logic can be found in Y. Asaoka et al. (2018).

3.1. CALET UH Data Selections

This analysis looks at flight data collected from 2015 October 13 to 2023 November 30, representing approximately 8 yr of on-orbit operation. The data analysis follows procedures shown previously in B. Rauch et al. (2017), A. Ficklin et al. (2021), and W. V. Zober et al. (2021a), where all events must meet signal thresholds for the UH trigger to be satisfied. These thresholds result in the loss of events for elements below $Z = 10$, but the overall efficiency is nominally consistent with the HE trigger for heavier elements. For data-quality purposes, the events that occur on the edges of CHDX and CHDY are removed, as those regions of the detector suffer from lower statistics and, as such, have reduced confidence in the accuracy of the correction factors. Events that are tagged as passing through the structure of the ISS are removed to reduce the number of events that may have interacted with the structure of the ISS and an unknown amount of mass. Data that correspond to times when the ISS is reoriented are also removed from the final data set.

3.2. CHD UH Response Corrections

The CALET instrument has many calibrations applied to the pipeline-produced standard data set that is optimized to measure the energy spectra of the abundant elements lighter than UHGCRs. However, these UH measurements have significantly lower statistics and are extremely sensitive to

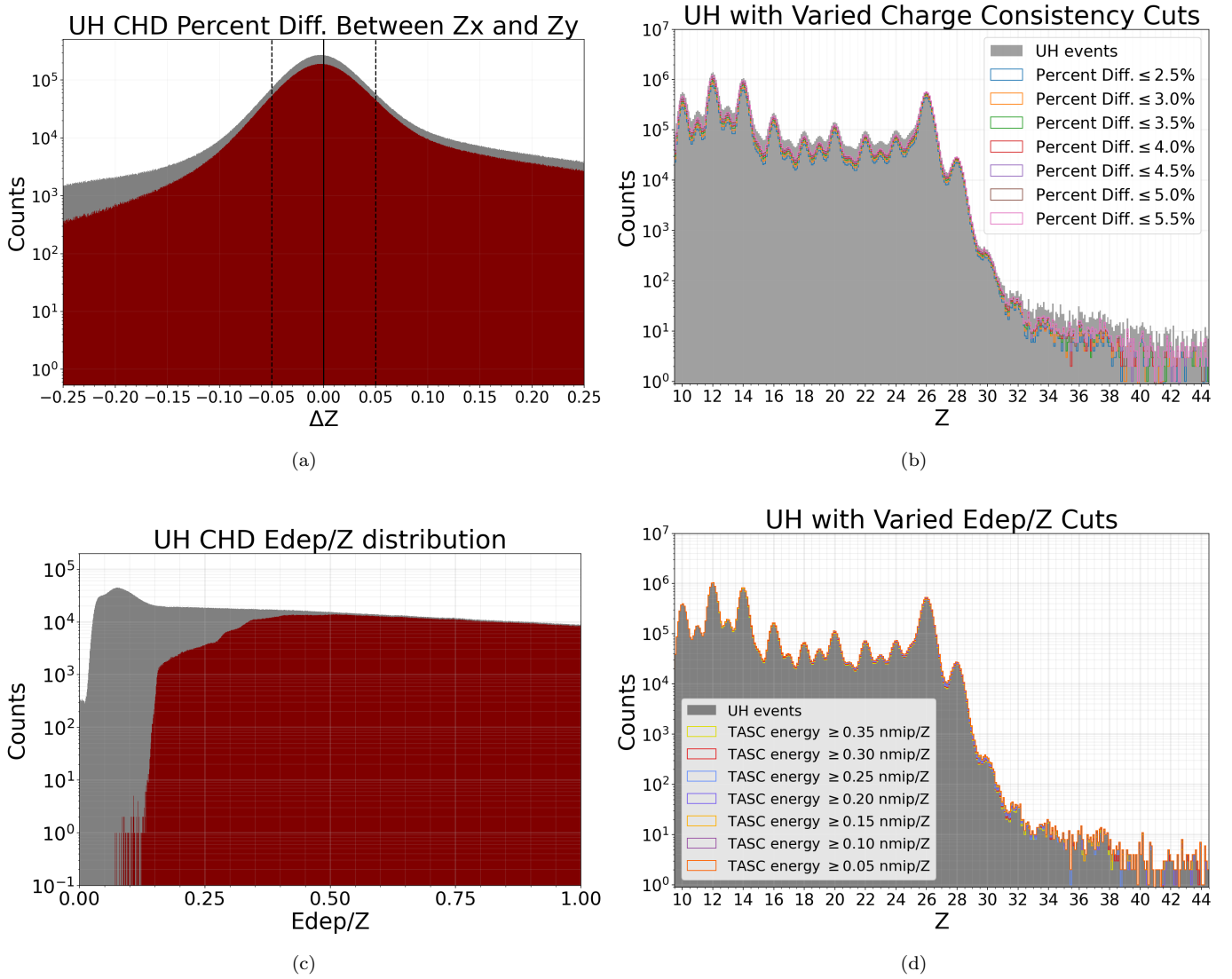

Figure 4. (a) Histogram showing percentage difference in CHDX and CHDY. The gray histogram depicts all UH-trigger events. The maroon histogram shows events with deposited energy in the TASC > 3.718 GeV and not on the CHD edge. Binned in 0.02% increments. (b) Histogram showing how changes in maximum percentage difference in charge consistency impact relative peak height and peak shape. (c) Histogram showing how event counts vary with deposited energy/Z. The gray histogram depicts all UH-trigger events. Maroon histogram shows events with a deposited energy >3.718 GeV and not on the CHD edge. The histogram has a fine binning resolution of 0.005 GeV/Z. (d) Histogram showing how changes in minimum deposited energy affect the relative peak height and peak shape. Higher minimum deposited energy creates clearer peaks at the cost of event statistics.

small percentage differences in charge measurements. UH analysis events have significantly higher detector signals as the signal grows with Z^2. This means that the locations of clear peaks to validate charge cuts, such as those made in other CALET analyses, cannot be directly used and one must instead use the detector response from those lower Z values to extrapolate charge-dependent shifts in detector response due to position-dependent (i.e., due to light propagation and absorption and material defects) and time-dependent (i.e., small changes in the gain due to temperature fluctuations) instrumental effects.

These corrections need to be done only for the CHD and not the IMC and the TASC, as the UH track determination and the TASC data themselves are sufficiently accurate for use.

3.2.1. Position-dependent Response Corrections

To complete these secondary UH calibrations, multiplicative correction factors were derived that rely on noninteracting $_{26}$Fe events to generate corrections optimized for the UH analysis. In previous iterations of this analysis, this has been done by dividing the paddle into 42 $\sim 1/3$ paddle-width segments along their lengths and normalizing signals in each segment by multiplying by the ratio of the CHD layer $_{26}$Fe mean signal divided by the segment mean signal (W. V. Zober et al. 2021a). By sampling events that are known to pass through in a particular paddle segment, the relative response of the charge measurement can be determined in that segment with high confidence. This was later expanded to add in a second high statistic peak, $_{14}$Si, and change the multiplicative correction to a weighted linear correction that applied only the silicon correction factor to events below the silicon peak, applied the $_{26}$Fe factor to all events above the $_{26}$Fe peak, and applied a weighted correction to events between the two peaks. The work shown here modifies this correction by adding in the peaks for $_{10}$Ne and $_{12}$Mg to generate a four-peak average correction factor.

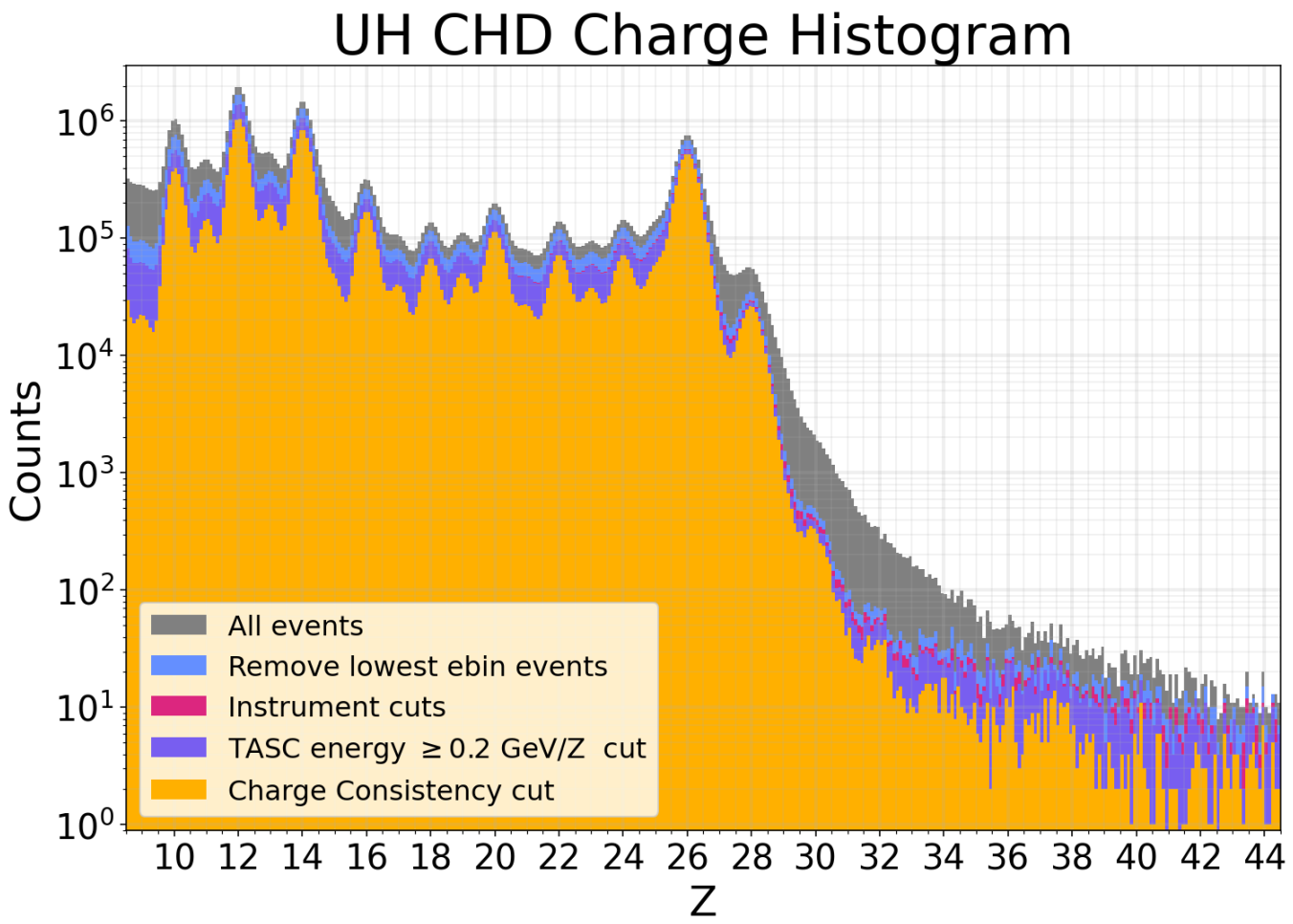

Figure 5. The TASC UH data set, with successive cuts applied. A minimum deposited energy in the TASC of 3.718 GeV removes the lowest three energy bins, the instrument cuts of which include removing the outer edge of the CHD, events that interact with the ISS and from bad timestamps, a minimum deposited energy in the TASC as a function of Z (Edep/Z), and the 4% charge consistency cut.

In this analysis, each CHD paddle is divided along its length into 42 segments that are each $1/3$ of the width of the CHD paddle. This step samples all events that pass through each segment and selects those that have $\geqslant$98% of the signal in only that segment, performing a Gaussian fit for the mean signal in that segment for $_{10}$Ne, $_{12}$Mg, $_{14}$Si, and $_{26}$Fe. The charge dependence of this correction was investigated, and no significant trend was found. Therefore, the average of these four ratios is taken and used as the correction factor.

3.2.2. Time-dependent Response Corrections

The CALET UH data show modulations that occur on various timescales, including a 21 day and 55 day modulation due to the precession of the ISS orbit. A time-dependent response normalization is performed to remove these modulations and is performed similarly for the position-based correction. The data are divided into 1 week time intervals for $_{10}$Ne, $_{12}$Mg, $_{14}$Si, and $_{26}$Fe. These time corrections (using the average from the four peaks, similar to the procedure for the position dependence) are done by normalizing the individual CHD paddles to the full layer mean signal.

3.2.3. Energy-dependent Response Corrections

After applying position and time corrections, the amount of energy deposited by each event in the TASC, Edep, is used in the analysis. As stated previously, the calorimeter can fully contain electron-induced showers up to 10s of TeV, but for nuclei the fraction of deposited energy decreases. To get the kinetic energy of an event used for flux measurements, Monte Carlo simulations are required to unfold the deposited energy. However, in this analysis, there are insufficient statistics for the flux measurement of UH elements, and so since exact kinetic energies are not needed, a simple correction using deposited energy in the charge assignment is made.

Particle interactions from GCRs are complex. Interactions occur with the detector as cosmic rays pass, causing energy losses. For heavy particles, such as UHGCRs, ionization energy deposit is described by the Bethe-Bloch equation. As CALET's CHD is composed of Eljen EJ-204 plastic scintillators, the probabilistic mean energy deposited for any Z is determinable.

The light emitted by scintillating material for an interacting charged particle is a portion of the energy deposited E/dx, and light yields are affected by material-dependent processes. The particle interactions that cause scintillation have a saturation

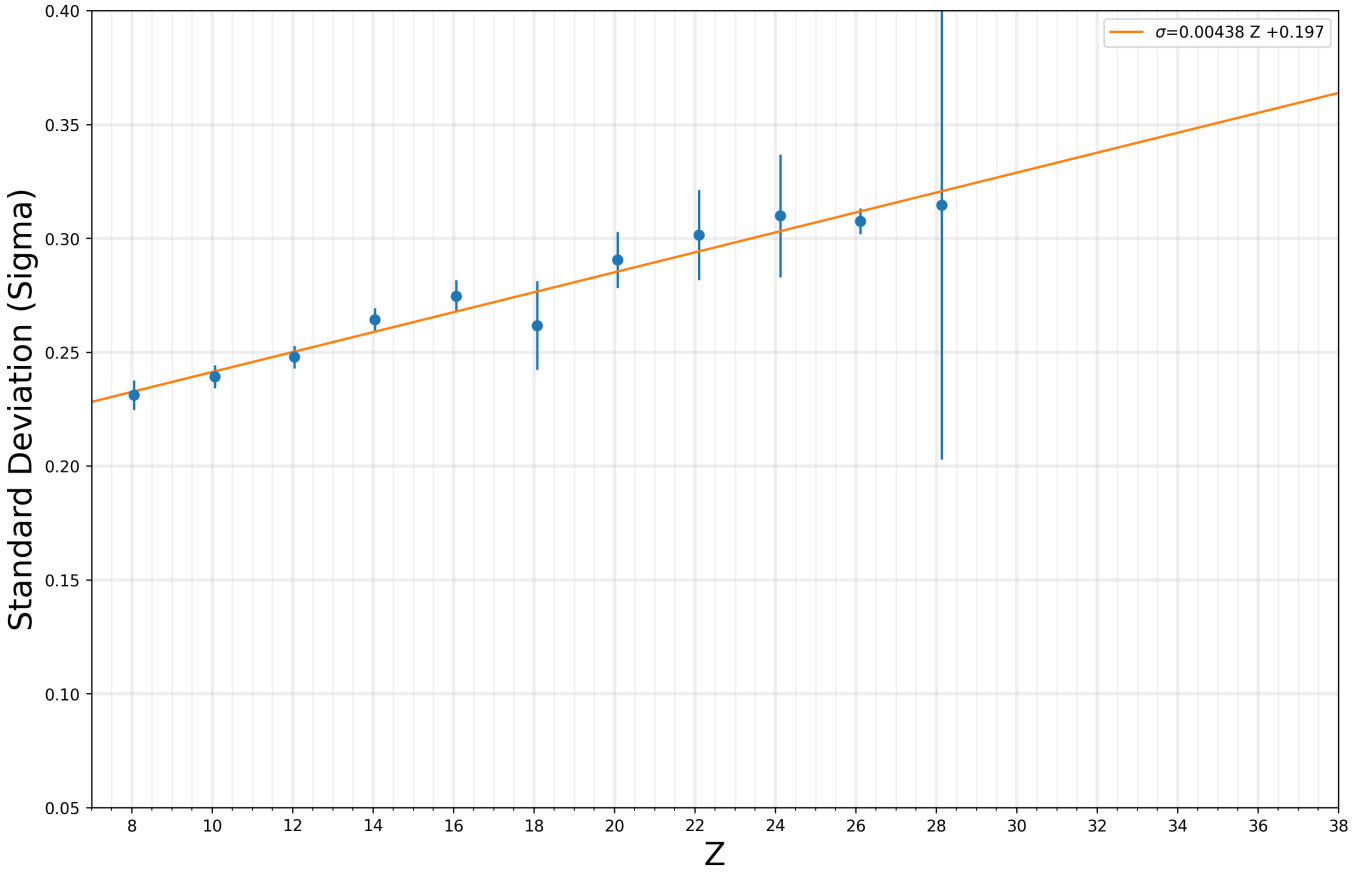

Figure 6. Linear fit on the sigmas from the initial fit. Data points for even Z values shown here are from the previous fit. The following fits in the routine are required to have a peak width within 5% from this linear best fit.

limit where the scintillator cannot convert energy into light, and energy is lost to other effects such as knock-on electrons and thermal radiation. This saturation is charge dependent (G. Tarle et al. 1979).

The difficulty in modeling the saturation effect comes from the uncertainty in knock-on electron interactions. Electrons knocked free in the initial interaction can transport energy away from the primary deposit. To account for this, we use the common form of the Tarle function,

$$\text{Signal} = \frac{\text{AZ}^2}{1 + \text{BZ}^2} + \text{CZ}^2. \quad (1)$$

With Equation (1), the CHD signal can be converted into charge units, and by leveraging CALET's excellent energy resolution, the UH events are divided into 50 similarly sized event bins based on the deposited energy in the TASC, ~80,000 $_{26}$Fe events (26 ± 0.15 charge units (e)). A multi-Gaussian peak fit is done for the CHDX and CHDY event histograms in each energy bin.

The maximum likelihood multi-Gaussian peak fit routine shown in Figure 3 does the following: It first identifies the peak locations of signal for each element shown in Figures 3(a) and (b) from $Z = 6$ to $Z = 28$. These plots show an unscaled charge based on taking the square root of the signal. Some peak locations are resolved with more clarity and accuracy than others, but so long as the majority of points follow a consistent pattern, the routine can resolve sections with poorer peak resolution.

After this step, a Tarle model fit is performed with the peak positions and the equivalent charge number for CHDX and CHDY (Figure 3(c)). To give constraints on the fit and aid in the prevention of misassigned charge numbers for Z in the UH regime, the routine has strict rules for the maxima and minima of parameters to keep the resulting equation and expected peak positions for $Z > 30$ consistent with the fits used in the CALET $_{26}$Fe and $_{28}$Ni analyses (O. Adriani et al. 2021, 2022). These fits are all examined to make sure they properly converge.

This process then returns a determined Z from the model fit. This is shown in Figure 3(d), with the assigned charge for CHDX in blue and CHDY in red, and the average Z overlaid in green shading.

3.3. Determination of Data-quality Cuts

After corrections, additional data selection cuts are made to address the issues that appeared in the two correction factors and charge assignment.

The first cut is a rejection of all events with deposited energy in the TASC that are $\leqslant$2.35 GeV. These events constitute the first three bins from the Tarle charge assignment process. All three of these bins suffered from charge smearing that made peak identification impossible, which could result in incorrect charge assignment to events. This cut accounts for a ~15% reduction of events in the data set.

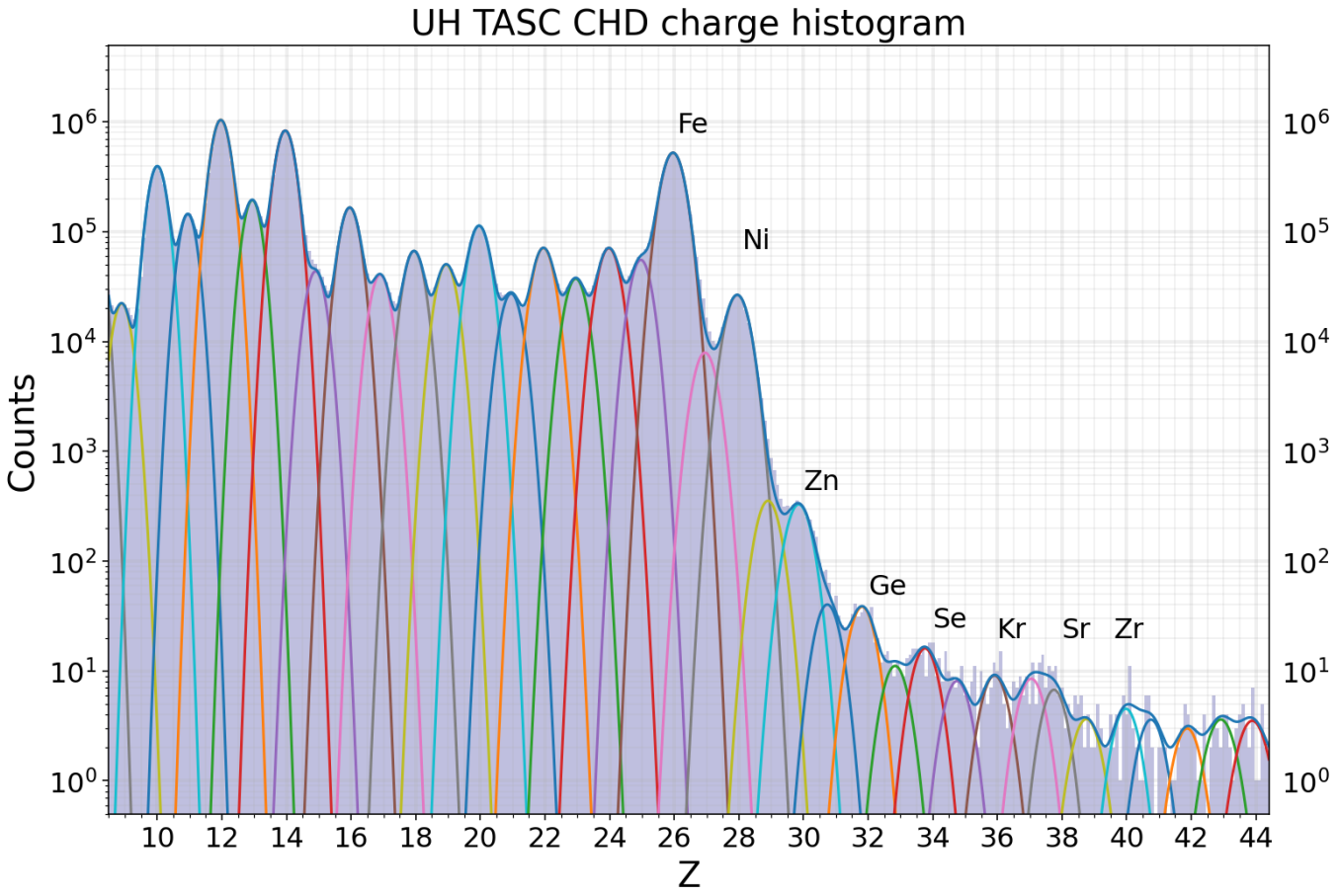

Figure 7. The results of the multi-Gaussian fit procedure for the TASC UH abundances. The number of events within the full fit is roughly identical to the number in the histogram (<1% difference between fit and histogram).

The next cut is the requirement that the charge determination of events CHDX and CHDY should be within a few percent of each other. An optimal charge consistency cut was selected by analyzing the percentage differences of all events in the data set and comparing them to simulations.

In Figure 4(a) the distribution of events as a function of percentage difference is shown, and Figure 4(b) shows how minor changes in percent difference modify the event histogram.

Figure 4 shows that the distribution of percentage differences is not symmetric and that cut selection impacts the UH event distribution in a variety of ways, so a good cut needs to occur below that asymmetry. The dashed lines added in Figure 4 at $\pm 0.05\%$ highlight where the asymmetry in CHDX and CHDY approximately begins and constrain the maximum percentage difference.

The next data cut examines how the deposited energy varies over the range of Z in Figure 4(c). The event distribution of all TASC events is shown in the gray histogram; these data show a rapid rise into a peak and then have a gradual drop-off that becomes approximately linear. The histogram that omits the first three deposited energy bins (shown in red) does not have a low Edep/Z peak but rather rises with energy. From this a cutout of events less than $\sim$0.20 Edep/Z is identified. The effects of varying this value are visible in Figure 4(d). The effects of these four cuts applied successively are shown in Figure 5.

The effects of these cuts are accounted for in a set of correction factors in the final analysis.

4. Results

4.1. Initial Analysis

To find abundances for the UH TASC analysis, the methodology implemented in the SuperTIGER analysis in (N. E. Walsh 2020; N. E. Walsh et al. 2022) is used. This methodology performs multiple iterations of fitting a maximum likelihood, multipeak Gaussian function to the histogram of data. This multipeak function is composed of 50 Gaussian functions with integer spacing between peaks for $Z \leqslant 50$. Not every peak may be used in this analysis, since high Z elements are incredibly rare, acceptance angle decreases at the higher Z from detector saturation, and the signal from the lowest Z is well below the trigger threshold. However, all Z are treated as if they could exist in this analysis. The routine requires the individual peaks to center near the integers, with constant spacing between peaks and peak widths allowed to linearly vary with Z.

In the first iteration of the fit, peak height is initialized with a range around the minimum and maximum local values in the histogram. The only constraint in the fit is that there must be a baseline spacing between peaks around 1.00 ± 0.05 e, with the individual peaks allowed to vary up to ± 0.15 e from that constant value.

Table 1
Abundances of Nuclei

Z (1)	N (2)	Fit E± (3)	Var E_+ (4)	Var E_- (5)	Stat E_+ (6)	Stat E_- (7)	Combined E_+ (8)	Combined E_- (9)
14	2222398	8311	36510	31343	912	911	37455	32439
15	119178	936	1702	2363	209	208	1954	2551
16	461162	1657	7624	5898	408	407	7813	6140
17	114650	405	1958	1463	202	201	2010	1531
18	191473	666	3074	2256	259	258	3156	2366
19	146273	501	2316	1612	224	223	2380	1703
20	335429	1131	4949	3579	337	336	5088	3769
21	82078	272	1200	942	166	165	1242	994
22	216188	710	3315	1927	267	266	3401	2071
23	115853	426	1766	1213	194	193	1828	1300
24	222829	1024	3554	1725	267	266	3709	2024
25	166068	553	2378	2174	236	235	2453	2255
26	1693464	5230	24275	13778	724	723	24842	14756
27	25960	146	1397	618	89.9	88.9	1407	642
28	90131	265	1105	808	163	162	1148	866
29	1195	3.54	16.8	12.1	19.8	18.8	26.3	22.7
30	1167	6.11	19.5	8.7	19.1	18.1	28.0	21.0
31	139	0.6	2.21	1.74	7.4	6.31	7.75	6.58
32	134	0.73	0.5	2.16	7.26	6.17	7.31	6.57
33	39.5	0.23	0.92	0.68	4.44	3.28	4.54	3.36
34	57.8	0.21	0.59	1.96	5.1	3.96	5.14	4.42
35	29.5	0.13	0.68	0.26	3.97	2.78	4.03	2.8
36	33.5	0.16	0.44	0.85	4.13	2.95	4.16	3.08
37	31.8	0.12	0.41	0.23	4.04	2.85	4.06	2.86
38	23.5	0.18	0.52	0.19	3.74	2.52	3.78	2.54
39	13.9	0.04	0.41	0.45	3.1	1.81	3.12	1.87
40	16.2	0.11	0.18	0.15	3.3	2.04	3.3	2.05
41	13.0	0.04	0.19	0.19	3.09	1.8	3.09	1.81
42	11.0	0.07	0.2	0.2	2.93	1.63	2.94	1.64
43	14.5	0.04	0.2	0.09	3.09	1.8	3.09	1.81
44	14.3	0.04	0.52	0.07	3.07	1.78	3.11	1.78

Note. CALET UH analysis abundances from the multi-Gaussian fit routine. For each element of atomic number Z (column (1)) with the determined abundances under each peak (column (2)), the error is from a combination of the fitting routine error (column (3)), a systematic error based on how abundances change with varying minimum energy and charge consistency cuts (columns (4) and (5)), the Poissonian statistics error as determined by Gehrels (columns (6), (7)), and the final error combined in quadrature (columns (8), (9)).

The second step is a linear fit to the even-Z sigma values up to $Z = 28$ (Figure 6). Peak resolution is expected to vary linearly as a function of Z. By fitting the even sigmas from 8 to 28, the predicted sigma widths can be extrapolated to higher Z values. Odd peaks are omitted from this step to remove noise caused by poor fitting on peaks that do not have clear maxima, such as $_{15}$P.

The next fit is a multi-Gaussian with an additional constraint on sigma, such that all sigmas must be within 5% of the expected sigma from the linear equation for all Z values. Once this fit is completed, a final fit is performed with fixed sigmas and peak positions from the previous fit, only allowing amplitude to vary (Figure 7). To allow all peaks to return reasonable values, unidentifiable peaks are allowed a wider limit on the range of acceptable values. The process is done this way to obtain a converging fit in a reasonable amonut of time, with defined error bars on the amplitudes in the fit. The raw abundances found by this routine are shown in Table 1.

4.1.1. Error Methods

The initial error for the analysis is determined from three sources. The first source is the fitting error as output from the fitting routine. This is a derived value from the covariance matrix of the final fit. The second source of the error is defined as a variational error, Var_$E_\pm$. This error is derived from the choices of cuts in the analysis. This is defined by slightly varying the event selection criteria based on percentage difference (Figure 4(b)) and minimum deposited energy in the TASC as a function of Z (Edep/Z) (Figure 4(d)). The maximum and minimum differences for each peak from the fit shown in Figure 7 are used and then normalized for the error on the abundances.

The third source is a Poissonian error derived by N. Gehrels (1986) Equations (7) and (12), with $S = 1$ and N as the number of events for the upper (Equation (2)) and lower (Equation (3)) statistical error. These three errors are then combined in quadrature and are all shown in Table 1.

$$\text{Stat} \quad E_+ \approx 1 + \sqrt{N + \frac{3}{4}} \tag{2}$$

$$\text{Stat} \quad E_- = N\left[1 - \frac{1}{9N} - \frac{1}{3\sqrt{N}}\right]^3 \tag{3}$$

4.2. Corrections Based on Analysis Methods

Note these values are not final, as cuts performed in the analysis add several systematic discrepancies to the results.

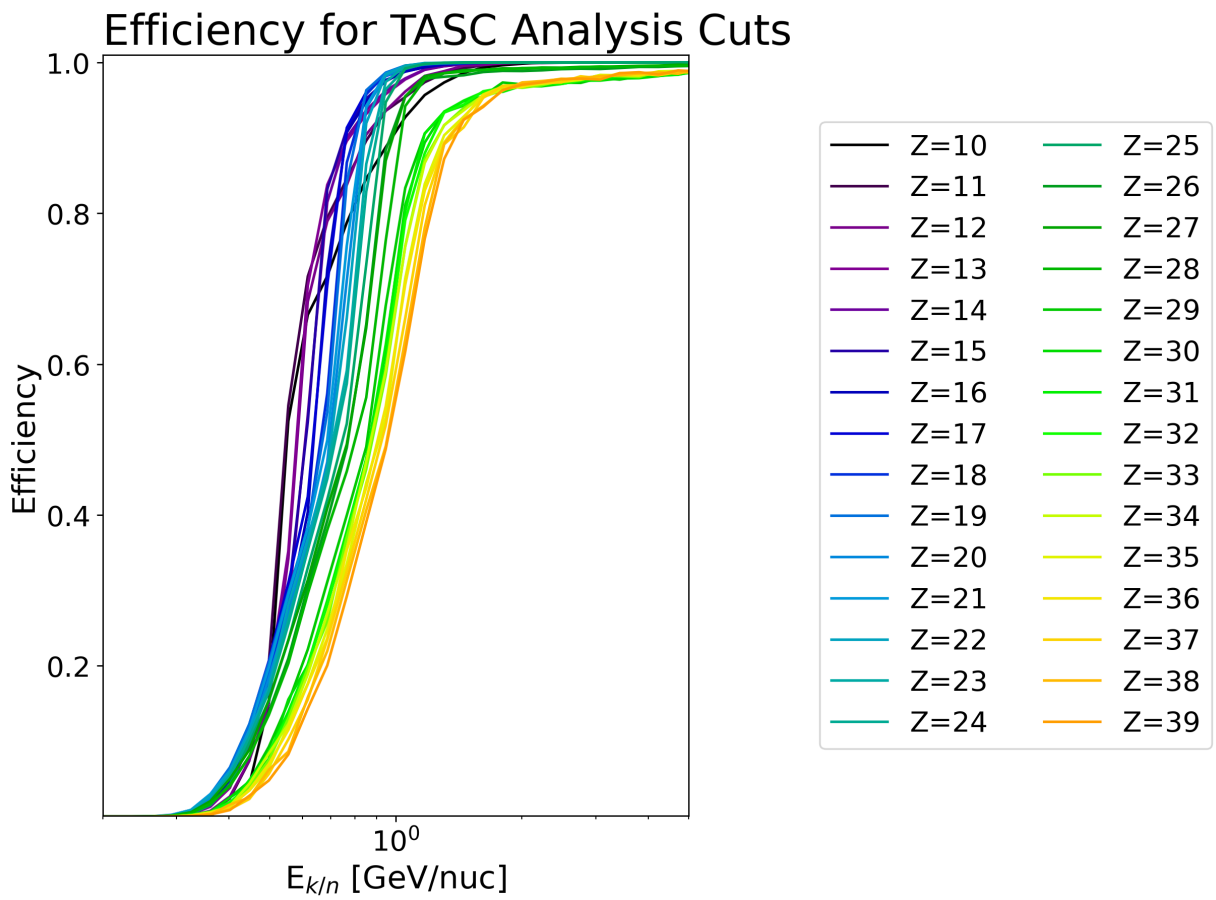

Figure 8. Efficiences of each nuclei as a function of energy. Simulated data have identical cuts applied for the analysis. Efficiencies are normalized by fluxes derived from data published by ACE-CRIS (K. A. Lave et al. 2013) and HEAO-3-C2 (J. J. Engelmann et al. 1990). The fluxes for elements heavier than $_{26}$Fe are assumed to be of the same form as $_{26}$Fe.

Events have been removed based on minimum energy, charge consistency, and the physical constraints of the detector.

4.2.1. Correction for Selection Efficiencies

To correct for species- and energy-dependent losses resulting from these cuts, we determine the corresponding efficiencies from Monte Carlo simulations. These simulations are performed with the EPICS (K. Kasahara 1995) package, using DPMJET-III (S. Roesler et al. 2001) for hadronic interactions and a detailed instrument mass model. Events are generated for species $_{10}$Ne to $_{39}$Y over 1–550 GeV, and the same selections are applied as in the flight data analysis. From this we calculate the survival fraction for each species in 40 bins of energy (Figure 8).

As the measurement of abundances is completed without a determination of primary energies, it is necessary to assume the spectral shape of each species to propagate the energy-dependent efficiencies for a scaling factor appropriate for our result. Elemental fluxes are taken from ACE-CRIS (K. A. Lave et al. 2013) and HEAO-3-C2 (J. J. Engelmann et al. 1990) for $_{10}$Ne through $_{26}$Fe, and we assume the spectral shape of $_{26}$Fe for heavier elements.

A correction factor is derived for each species as the ratio of the flux multiplied by the efficiency integrated over the energy range of interest to the flux multiplied by the efficiency integrated over the entire energy range.

4.2.2. Charge-changing Interactions

The interaction rate in EPICS simulations is based on the cross sections of interacting nuclei. However, the cross sections for the majority of UH nuclei in CALET's energy range are not measured, so cross sections are modeled based on Z, nuclear radii, and energy. To determine the systematic impact of relying on EPICS and DPMJET simulations, a brief study on interactions in other simulation packages and analytical methods was completed.

To do this check, the survival fraction of each Z passing through the first layer of the CHD is calculated with multiple approaches. First, an analytical method that is based on the average path length traversed within the material of CHDX and the interaction mean-free paths for each Z. The total charge-changing sections used in the mean-free path calculations are from the work of B. S. Nilsen et al. (1995).

Simulations were completed using two alternative simulation packages in Geant4. The standard Geant4 simulation uses the shielding physics list, but the default radius function is a piecewise function that results in a large break in particle radii that is not consistent with other simulation packages or analytical models. As such, this analysis has opted to use two different Geant4 simulations—one that is based on rms charge radii and another that is based on the radii function within the DPMJET code. The resultant survival fractions, and the

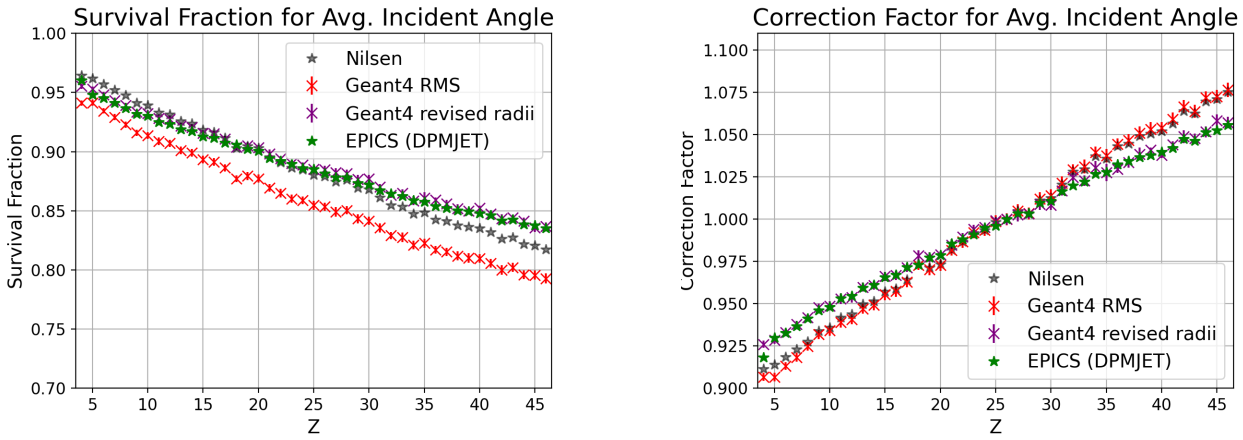

(a) (b)

Figure 9. (a) Survival fractions as determined by simulations in EPICS and Geant4, and the analytical model from B. S. Nilsen et al. (1995). (b) The derived correction factors from the survival fractions relative to $_{26}$Fe.

Table 2
Final Abundances after Corrections

Z (1)	N (2)	Combined E (+) (3)	Combined E (−) (4)
14	3044044	42898	36024
15	172388	4813	5340
16	639568	8982	7186
17	160342	2404	1778
18	261227	3842	2787
19	194411	2879	2115
20	428136	5824	4379
21	105700	2322	2030
22	258099	3909	2391
23	144661	2134	1448
24	278195	4114	2767
25	208703	3010	3386
26	1969419	29157	16888
27	31503	1216	989
28	101712	1603	1031
29	1433	47.0	43.2
30	1192	29.5	24.4
31	90.4	6.64	5.42
32	127	7.91	6.64
33	34.4	4.46	3.33
34	51.1	5.32	4.14
35	31.5	4.33	3.12
36	31.8	4.33	3.1
37	33.9	4.54	3.32
38	28.0	4.19	2.95
39	13.2	3.44	2.19
40	18.6	3.66	2.41
41	10.5	3.15	1.79
42	10.5	3.15	1.84
43	12.6	3.25	1.93
44	12.9	3.32	2.04

Note. Corrected CALET UH analysis abundances for each atomic number (Z; column (1)) with the final abundances (column (2)). The combined upper (column (3)) and lower (column (4)) uncertainties include all previously shown corrections.

survival fractions from EPICS, are all shown in Figure 9(a). A correction factor is generated from the inverse of the survival fractions relative to $_{26}$Fe. This is shown in Figure 9(b). By normalizing to a correction factor that is relative to $_{26}$Fe, differences in scaling factors can be neglected and distinct trend lines between individual models can be seen. An example of this is in the overlap of the GEANT4 rms and Nilsen's model.

This also allows for the differences between the various simulation packages and the analytical model to be incorporated into the systematic error on the CALET relative abundances. This is done by tracking the maximum and minimum correction factors across all models for each respective Z and applying the difference from EPICS to the upper and lower bounds of the error.

4.2.3. Geomagnetic Corrections

A final correction is applied to account for the geomagnetic screening of events. This correction is required to directly compare to other local space instruments. This is done by using the approximate energy per nucleon to be detected in this analysis (energy for 50% efficiency; Figure 8) for each nuclear species and converting it to units of magnetic rigidity. The fraction time above this geomagnetic rigidity is calculated using vertical cutoff rigidity for each minimum energy over the ISS orbit. These values are then normalized to the on-orbit time for $_{26}$Fe and used as a multiplicative factor.

4.3. Final Results of the Analysis

The final results are shown in Table 2. With the corrections shown, CALET is in good agreement with the results from several other experiments. In Figure 10, the CALET UH abundances for $14 \leqslant Z \leqslant 44$ are compared to HEAO, SuperTIGER, and ACE-CRIS abundances.

For $Z > 26$ the discrepancies with odd peaks reading out higher than results from other experiments remain. For this region, the relative abundances of odd–even element pairs are shown in Figure 11. This plot shows the TASC abundances in excellent agreement with published values from SuperTIGER and ACE-CRIS. This in turn informs us that while the individual peaks may vary from expected values due to poor charge resolution, the overall results are accurate.

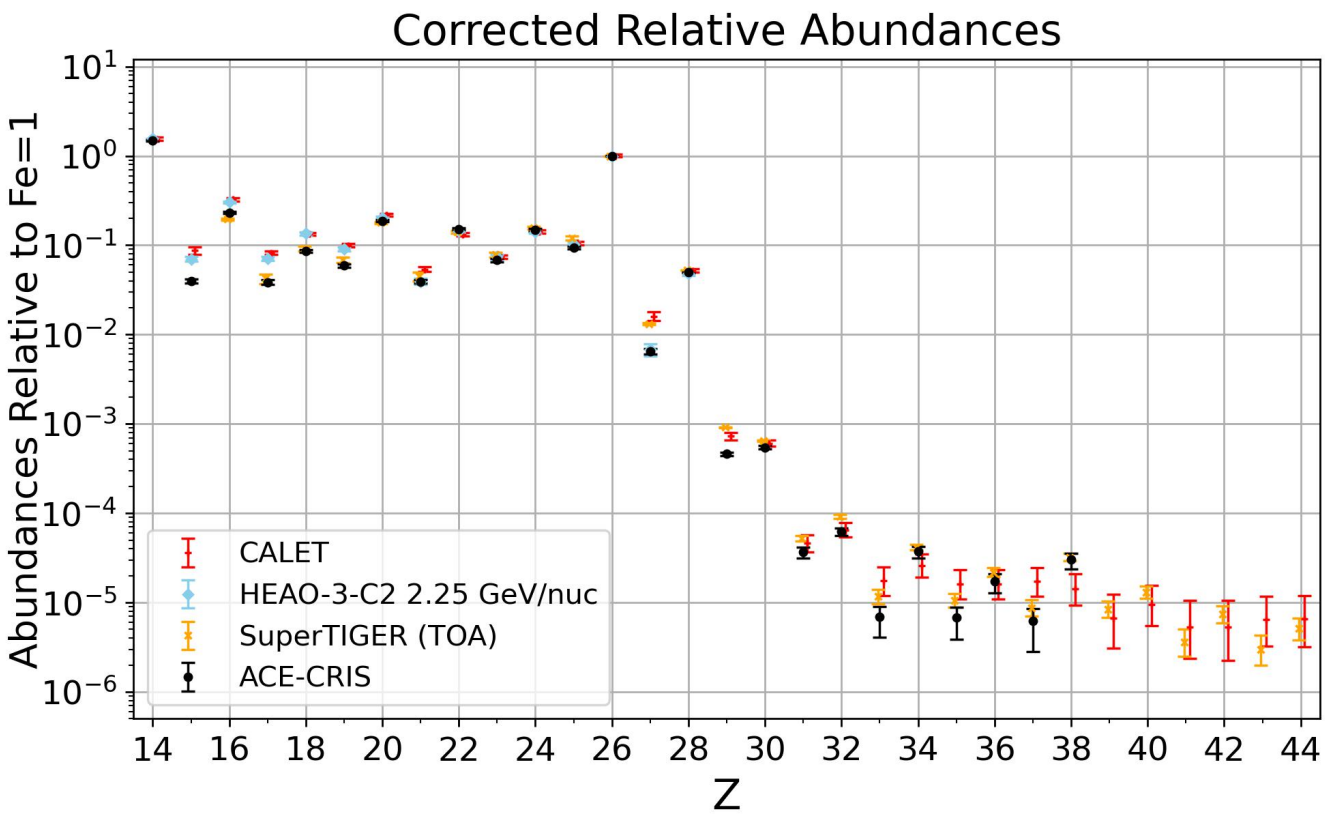

Figure 10. Corrected CALET relative abundances from Table 2 and plotted alongside results from several other experiments. For lower Z, CALET is able to be compared to HEAO-3-C2 (J. J. Engelmann et al. 1990), the SuperTIGER top of instrument (N. E. Walsh et al. 2022), and ACE-CRIS (M. H. Israel et al. 2018; W. R. Binns et al. 2022) abundances. The data used from ACE-CRIS and HEAO-3-C2 are the propagated source abundances.

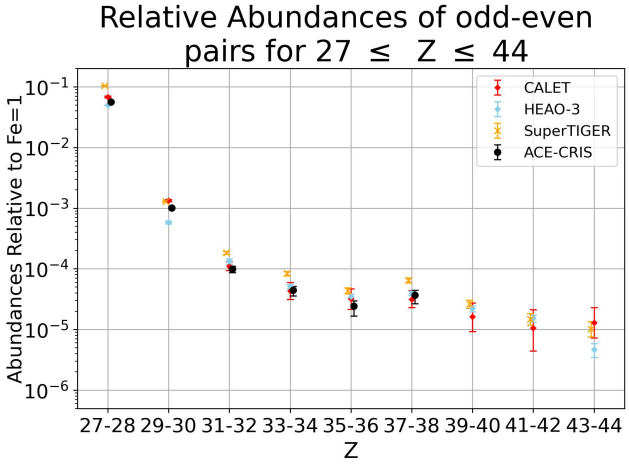

Figure 11. The relative abundances of the odd–even element pairs compared to abundances from HEAO-3 (W. R. Binns et al. 1989), ACE-CRIS (W. R. Binns et al. 2022), and SuperTIGER's top-of-atmosphere abundances (TOA; N. E. Walsh et al. 2022).

5. Conclusions

CALET has measured the cosmic-ray abundances in the $14 \leqslant Z \leqslant 44$ charge range, providing complementary measurements to ACE-CRIS, SuperTIGER, and HEAO-3-C2. The energy ranges of these experiments are moderately similar, with CALET's energy range extending from 0.5 to $\sim$300 GeV nuc^{-1}, SuperTIGER's energy range from $\sim$1 to 10 GeV nuc^{-1}, and HEAO-3's energy range from 0.6 to 35 GeV nuc^{-1} energies. ACE-CRIS's results are somewhat lower at 130–700 MeV nuc^{-1}.

CALET's results are consistent with all these experiments shown in the charge range shown. These observed differences are mostly due to low statistics on odd–even charge pairs and CALET's decreasing resolution at high Z.

While these results are not unique in this range, CALET provides a check for all other UH measurements and those for lower-Z elements in its range. The significant overlap with the SuperTIGER energy range with different systematics makes this comparison particularly significant through $Z = 44$.

However, the statistics for $Z > 28$ events are not yet at the point where peak identification is consistent. With the CALET mission, which is expected to continue for several years (potentially through the end of the ISS), greater statistics from the extended operations will provide the opportunity to revisit this analysis with a significantly improved UH data set and allow for better statistical resolution on the fitting routine and higher accuracy in the energy binning. Additionally, for CALET there is the potential to perform an HE-trigger analysis of the data and be able to determine the abundances of all Z values in CALET's range. A secondary analysis with an alternative trigger would also allow for exploration into potential Z-dependencies in trigger efficiencies and sampling biases as a function of Z based on rigidity selections and interaction fraction.

Acknowledgments

CALET is currently approved to continue operating through 2030. We gratefully acknowledge JAXA's contributions to the development of CALET and to the operations aboard the JEM-EF on the International Space Station. We also wish to express our sincere gratitude to Agenzia Spaziale Italiana (ASI) and NASA for their support of the CALET project. In Japan, this work was supported in part by JSPS Grant-in-Aid for Scientific Research (S) Nos. 26220708, 19H05608, and 24H00025; JSPS Grant-in-Aid for Scientific Research (B) No. 24K00665; and by the MEXT-Supported Program for the Strategic Research Foundation at Private Universities (2011–2015; No. S1101021) at Waseda University. The CALET effort in Italy is supported by ASI under agreement 2013-018-R.0 and its amendments. The CALET effort in the United States is supported by NASA through grants NNX16AC02G, NNX16AB99G, NNX11AE 06G, and 80NSSC20K0397. A.B. acknowledges support from NASA under award number 80GSFC24M0006.

ORCID iDs

O. Adriani https://orcid.org/0000-0002-3592-0654
Y. Akaike https://orcid.org/0000-0002-9489-1515
K. Asano https://orcid.org/0000-0001-9064-160X
Y. Asaoka https://orcid.org/0000-0001-6440-933X
E. Berti https://orcid.org/0000-0002-5841-7760
P. Betti https://orcid.org/0000-0002-7097-165X
G. Bigongiari https://orcid.org/0000-0003-3691-0826
W. R. Binns https://orcid.org/0000-0001-6110-3407
M. Bongi https://orcid.org/0000-0002-6050-1937
P. Brogi https://orcid.org/0000-0001-7953-0271
A. Bruno https://orcid.org/0000-0001-5191-1662
N. Cannady https://orcid.org/0000-0003-2916-6955
G. Castellini https://orcid.org/0000-0002-0177-0643
C. Checchia https://orcid.org/0000-0003-1241-0413
M. L. Cherry https://orcid.org/0000-0003-2808-312X
G. Collazuol https://orcid.org/0000-0002-7876-6124
G. A. de Nolfo https://orcid.org/0000-0002-3677-074X
K. Ebisawa https://orcid.org/0000-0002-5352-7178
H. Fuke https://orcid.org/0000-0002-8071-3398
S. Gonzi https://orcid.org/0000-0003-4754-645X
T. G. Guzik https://orcid.org/0000-0001-6339-8261
K. Hibino https://orcid.org/0000-0001-9259-6371
M. Ichimura https://orcid.org/0000-0002-0052-4985
M. H. Israel https://orcid.org/0000-0002-8104-208X
K. Kasahara https://orcid.org/0000-0001-5611-3301
J. Kataoka https://orcid.org/0000-0003-2819-6415
R. Kataoka https://orcid.org/0000-0001-9400-1765
Y. Katayose https://orcid.org/0000-0003-4836-7621
N. Kawanaka https://orcid.org/0000-0001-8181-7511
Y. Kawakubo https://orcid.org/0000-0002-2064-3164
K. Kohri https://orcid.org/0000-0003-3764-8612
H. S. Krawczynski https://orcid.org/0000-0002-1084-6507
J. F. Krizmanic https://orcid.org/0000-0002-9690-9352
P. Maestro https://orcid.org/0000-0002-4193-1288
P. S. Marrocchesi https://orcid.org/0000-0003-1966-140X
A. M. Messineo https://orcid.org/0000-0001-7551-5613
S. Miyake https://orcid.org/0000-0002-3067-655X
A. A. Moiseev https://orcid.org/0000-0002-1273-9959
M. Mori https://orcid.org/0000-0003-2921-1592
N. Mori https://orcid.org/0000-0003-2138-3787
H. M. Motz https://orcid.org/0000-0003-1918-2177
K. Munakata https://orcid.org/0000-0002-2131-4100
S. Nakahira https://orcid.org/0000-0001-9307-046X
M. Negro https://orcid.org/0000-0002-6548-5622
J. F. Ormes https://orcid.org/0000-0002-7220-6409
S. Ozawa https://orcid.org/0000-0002-6700-5530
L. Pacini https://orcid.org/0000-0001-6808-9396
P. Papini https://orcid.org/0000-0003-4718-2895
B. F. Rauch https://orcid.org/0000-0002-1452-4142
S. B. Ricciarini https://orcid.org/0000-0001-6176-3368
T. Sakamoto https://orcid.org/0000-0001-6276-6616
M. Sasaki https://orcid.org/0000-0002-8273-116X
A. Shiomi https://orcid.org/0000-0002-2616-0059
F. Stolzi https://orcid.org/0000-0001-9266-8742
T. Terasawa https://orcid.org/0000-0003-2507-9803
S. Torii https://orcid.org/0000-0003-3363-3827
Y. Tsunesada https://orcid.org/0000-0001-9238-6817
E. Vannuccini https://orcid.org/0000-0002-8647-2804
K. Yamaoka https://orcid.org/0000-0003-3841-0980
S. Yanagita https://orcid.org/0000-0002-5837-8511
K. Yoshida https://orcid.org/0000-0001-6813-2665
W. V. Zober https://orcid.org/0000-0003-2961-8894

References

Abbott, B. P., Abbott, R., Abbott, T. D., et al. 2017, ApJL, 848, L12
Abbott, B. P., Abbott, R., Abbott, T. D., et al. 2017, PhRvL, 119, 161101
Adriani, O., Akaike, Y., Asano, K., et al. 2021, PhRvL, 126, 241101
Adriani, O., Akaike, Y., Asano, K., et al. 2022, PhRvL, 128, 131103
Aguilar, M., Alcaraz, J., Allaby, J., et al. 2011, ApJ, 736, 105
Akaike, Y., Adriani, O., Asano, K., et al. 2024, AdSpR, 74, 4353
Asaoka, Y., Akaike, Y., Komiya, Y., et al. 2017, APh, 91, 1
Asaoka, Y., Ozawa, S., Torii, S., et al. 2018, APh, 100, 29
Bandyopadhyay, A., Ezzeddine, R., Allende Prieto, C., et al. 2024, ApJS, 274, 39
Binns, W. R., Garrard, T. L., Gibner, P. S., et al. 1989, ApJ, 346, 997
Binns, W. R., Wiedenbeck, M. E., Rosenvinge, T. T. V., et al. 2022, ApJ, 936, 13
de Séréville, N., Tatischeff, V., Cristofari, P., Gabici, S., & Diehl, R. 2024, MNRAS, 530, 684
Ellison, D. C., Drury, L. O., & Meyer, J.-P. 1997, ApJ, 487, 197
Engelmann, J. J., Ferrando, P., Soutoul, A., et al. 1990, A&A, 233, 96
Epstein, R. I. 1980, MNRAS, 193, 723
Ficklin, A., Cannady, N. W., Rauch, B. F., Zober, W. V. & CALET 2021, ICRC (Berlin), 395, 069
Fujibayashi, S., Kiuchi, K., Wanajo, S., et al. 2023, ApJ, 942, 39
Gehrels, N. 1986, ApJ, 303, 336
Higdon, J. C., & Lingenfelter, R. E. 2005, ApJ, 628, 738
Israel, M. H., Lave, K. A., Wiedenbeck, M. E., et al. 2018, ApJ, 865, 69
Kasahara, K. 1995, ICRC (Rome), 1, 399
Lave, K. A., Wiedenbeck, M. E., Binns, W. R., et al. 2013, ApJ, 770, 117
Lingenfelter, R. E. 2019, ApJS, 245, 30
Lodders, K. 2003, ApJ, 519, 1220
Nilsen, B. S., Waddington, C. J., Cummings, J. R., Garrard, T. L., & Klarmann, J. 1995, PhRvC, 52, 3277
Patel, A., Metzger, B. D., Cehula, J., et al. 2025, ApJL, 984, L29
Rauch, B., Akaike, Y. & CALET 2017, ICRC (Busan), 301, 180
Rauch, B. F., Binns, W. R., Israel, M. H., et al. 2011, ICRC (Beijing), 6, 355
Rauch, B. F., et al. 2009, ApJ, 697, 2083
Roesler, S., Engel, R., & Ranft, J. 2001, in Advanced Monte Carlo for Radiation Physics, Particle Transport Simulation and Applications, ed. A. Kling et al. (Berlin: Springer), 1033
Sanuki, T., Motoki, M., Matsumoto, H., et al. 2000, ApJ, 545, 1135
Tarle, G., Ahlen, S. P., & Cartwright, B. G. 1979, ApJ, 230, 607
Torii, S., & Marrocchesi, P. S. 2019, AdSpR, 64, 2531
Walsh, N. E. 2020, PhD thesis, Washington Univ.
Walsh, N. E., Akaike, Y., Binns, W. R., et al. 2022, AdSpR, 70, 2666
Walsh, N. E., Akaike, Y., Binns, W. R., et al. 2021, ICRC (Berlin), 395, 118
Zober, W. V., Rauch, B. F., Ficklin, A., Cannady, N. W. & CALET 2021, ICRC (Berlin), 395, 124